buildings

MDPI

Article

Research on Damage Identification of Arch Bridges Based on Deflection Influence Line Analytical Theory

Yu Zhou [1,2,3,*], Meng Li [1], Yingdi Shi [1], Chengchao Xu [4], Dewei Zhang [1] and Mingyang Zhou [1]

1 College of Civil Engineering, Anhui Jianzhu University, Hefei 230601, China; limengrq@outlook.com (M.L.); syd000408@outlook.com (Y.S.); zhangdwe@outlook.com (D.Z.); myzhou991205@outlook.com (M.Z.)
2 School of Civil Engineering, Lanzhou Jiaotong University, Lanzhou 730070, China
3 National and Local Joint Engineering Laboratory of Building Health Monitoring and Disaster Prevention Technology, Anhui Jianzhu University, Hefei 230601, China
4 Hefei Zezhong City Intelligent Technology Co., Ltd., Hefei 230601, China; chengxu217@outlook.com
* Correspondence: yuzhou923@outlook.com

Abstract: There is no analytical solution to the deflection influence line of catenary hingeless arches nor an explicit solution to the deflection influence line difference curvature of variable section hingeless arches. Based on the force method equation, a deflection influence line analytical solution at any location before and after structural damage is obtained, and then an explicit solution of the deflection influence line difference curvature of the structural damage is obtained. The indexes suitable for arch structure damage identification are presented. Based on analytical theory and a finite element model, the feasibility of identifying damage at a single location and multiple locations of an arch bridge is verified. This research shows that when a moving load acts on a damaged area of an arch structure, the curvature of the deflection influence line difference will mutate, which proves theoretically that the deflection influence line difference curvature can be used for the damage identification of hingeless arch structures. This research has provided theoretical support for hingeless arch bridge design and evaluation. Combined with existing bridge monitoring methods, the new bridge damage identification method proposed in this paper has the potential to realize normal health status assessments of existing arch bridges in the future.

Keywords: hingeless arch; analytical solution; deflection influence line; differential curvature; damage identification

check for updates

Citation: Zhou, Y.; Li, M.; Shi, Y.; Xu, C.; Zhang, D.; Zhou, M. Research on Damage Identification of Arch Bridges Based on Deflection Influence Line Analytical Theory. *Buildings* **2024**, *14*, 6. https://doi.org/10.3390/buildings14010006

Academic Editor: Bartolomeo Pantò

Received: 3 November 2023
Revised: 12 December 2023
Accepted: 16 December 2023
Published: 19 December 2023

1. Introduction

Given that the hingeless arch bridge has the advantages of great overall rigidity, convenient construction and low maintenance cost, it is widely used in practical engineering. However, temperature changes, material shrinkage, structural deformation, pier displacement and other factors lead to the subsidence and cracking of the main arch ring. The occurrence of these conditions usually leads to a reduction in the local rigidity of the structure [1]. The main arch rib and main arch ring are the main load-bearing structures of arch bridges [2]. Once the arch rib or main arch ring is damaged, the bearing capacity of an arch bridge will decrease greatly, or the bridge may even collapse [3].

Therefore, locating the damage quickly and evaluating the extent of the damage of the hingeless arch structure has great practical significance [4]. The influence line is an inherent attribute of bridge structure which reflects the flexural rigidity distribution of the bridge structure and is often used for safety assessments of beam bridge structures. The bridge influence line can "scan" the flexural rigidity of the structure section in the form of a single point output response under global loading to realize rapid testing and an accurate evaluation of the bridge's structure [5]. Influence lines have been widely used in bridge engineering, such as rapid assessments of bridge load capacity [6], model revision [7], and bridge load bearing [8]. In recent years, methods based on influence line damage identification have been rapidly developed [9,10]. Fan et al. [11] proposed an identification method for the damage of displacement difference influence lines of tied-arch bridges, derived the displacement influence lines of tied-arch bridges with the force method equation and verified the effectiveness of those displacement difference influence lines in identifying suspender damage on arch bridges through the finite element model. Wang et al. [12] proposed an iterative fitting calculation method to accurately extract bridge influence lines from the dynamic responses of bridge structures. Zhang et al. [13] proposed a new method to identify local rigidity distribution by using microwave interference radar technology and rotation influence lines. Zhu et al. [14] proposed a quasi-static structural damage identification method based on a single sensor influence line and an empirical Bayesian threshold estimation. He et al. [15] derived an iterative calculation formula describing the relationship between the influence line and temperature based on the analytical formula of the influence line of a concrete beam bridge and verified the validity of the iterative calculation formula through experiments. Samim [16] showed that the two most commonly used methods for identifying influence lines are the same in the time domain (TD) and frequency domain (FD) through theoretical demonstrations and comparative tests and proposed a new method for identifying influence lines. Ge [17] proposed a visual high-precision displacement influence line measurement system based on a combination of a computer vision subsystem and a motion weighing device which can be used for bridge damage detection. Hazem [18] studied the accuracy of detecting structural damage characteristics by using the rotation influence line (RIL) and its derivatives. The above studies provide a theoretical reference for the application of influence lines to bridge rapid testing and damage identification [19,20], but research on the analytic theory of influence lines and their application to arch bridge structural damage identification is still limited, and the scientific and practical applications of arch bridge damage identification proved analytically need to be further explored [21]. Most active arch bridges are masonry arch structures. Due to the complex internal force distribution of masonry structures and the discrete mechanical characteristics of masonry materials [22], there are few reports on the application of damage identification [23]. Therefore, the damage identification method for hingeless arches based on an analytical solution of the deflection influence line is proposed in this paper. The principle of damage identification can be clarified based on analytic theory.

In this paper, the elastic center method is used to simplify the force method equation and approximate curve fitting to simplify the catenary curve integral. The analytical solution of deflection influence lines (DILs) is applicable to the hingeless arch of a variable section catenary, and the deflection influence line of an arbitrary section of a catenary hingeless arch structure after damage was analyzed. The deflection influence line difference curvature (DILDC) before and after the structural damage was derived, and the DILDC damage identification index was proposed. The accuracy of the analytical solution was verified by establishing a hingeless arch finite element model. The scientific and practical applications of the damage index in damage identification were verified using a mechanical model of a catenary hingeless arch. The effects of locating the measuring point, the extent of damage to the unit, the impact of environmental noise on DILDC identification and the feasibility of quantifying the damage extent were studied. The analytical solution for the damage identification of hingeless arches proposed in this paper provides a basis for damage analyses of hingeless arches. A comparison of the numerical simulation and analytical solution shows that the analytical solution has fairly high accuracy. The DILDC index proposed in this paper provides an explicit solution for quantifying damage in hingeless arches. This research provides theoretical reference for the engineering design and damage diagnosis of structures.

The technical route is illustrated in Figure 1.

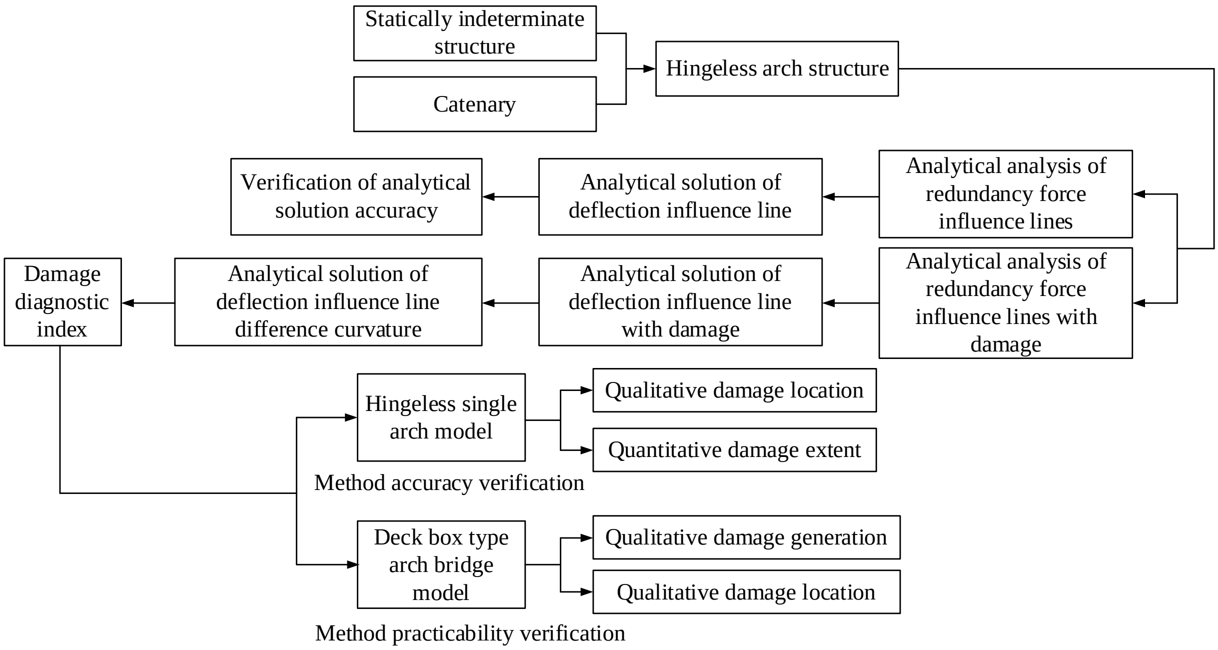

Figure 1. Technical route.

2. Deflection Influence Line Analytical Solution of Hingeless Arch in Non-Damaged Condition

2.1. Redundancy Force Influence Line of Variable Section Hingeless Arch in Non-Damaged Condition

The hingeless arch is divided into cantilever arches with left and right symmetry by the force method, which is illustrated in Figure 2. The A and B represent the left and right arch foot of the hingeless arch. The mid-span redundancy forces are x_1, x_2, and x_3. The elastic center method is used to simplify the force method equation, and the moving force coordinate of point C is set to x_{m}.

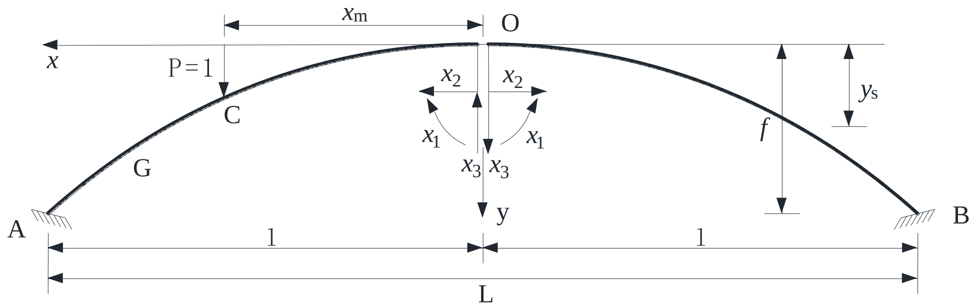

Figure 2. The basic system of the catenary hingeless arch.

The elastic center method is used to simplify the force method shown in Equation (1):

$$\begin{cases} \delta_{11}x_1 + \Delta_{1P} = 0 \\ \delta_{22}x_2 + \Delta_{2P} = 0 \\ \delta_{33}x_3 + \Delta_{3P} = 0 \end{cases} \tag{1}$$

The catenary arch axis equation is expressed as follows (Equations (2) and (3)):

$$y = f(chkx/l - 1)/(m - 1) \tag{2}$$

$$k = \ln(m^2 + \sqrt{m^2 - 1}) \tag{3}$$

where f denotes the height of the arch rib, m denotes the coefficient of the arch axis, and l denotes the half-span of the arch axis.

According to the Ritter formula, set the arch axis thickness as shown below (Equations (4)–(6)):

$$I = I_o / [(1 - x/l + nx/l) \cos \varphi] \tag{4}$$

$$\cos \varphi = \left[1 + (k^2 f^2 sh^2(kx/l)/(m-1)^2 l^2)\right]^{-1/2} \tag{5}$$

$$A = A_o[[1 - (1-n)x/l] \cos \varphi]^{-1/3} \tag{6}$$

where I_0 denotes the vault's moments of inertia, A_0 denotes the cross-sectional area of the rib vault position, n denotes the coefficient of change in the arch rib section and φ denotes the horizontal angle of the arch section.

The solution of the redundancy force influence line is the basis for solving the deflection influence line. The internal force and influence line of a section under the redundant force are depicted in Tables 1 and 2.

Table 1. Basic internal forces of the structure under the effect of redundancy forces.

Internal Force	Redundancy Force						Dummy-Moving Load		
	x_1		x_2		x_3			$x \le x_m$	$x > x_m$
Moment	$\overline{M_1}$	1	$\overline{M_2}$	$y - y_s$	$\overline{M_3}$	$\pm x$	M_p		$-(x - x_m)$
Axial force	$\overline{N_1}$	0	$\overline{N_2}$	$\cos \varphi$	$\overline{N_3}$	$\mp \sin \varphi$	N_p	0	$\sin \varphi$
Shear force	$\overline{Q_1}$		$\overline{Q_2}$	$\pm \sin \varphi$	$\overline{Q_3}$	$\cos \varphi$	Q_p		$\mp \cos \varphi$

(Note: When the section is calculated in the left half arch, the aforementioned symbol is utilized, and when the right half arch is taken, the following symbol is utilized).

Table 2. Analytical solution of redundancy force influence line.

Parameter	Significance	Fundamental Mechanical Expression	Practical Analytical Solution
y_s	Elastic center	$\frac{\int_S y ds}{\int_S ds}$	$y_s = \frac{2f\left[nk(m^2-1)^{1/2} + (1-n)(m-1) - k^2(1+n)/2\right]}{k^2(m-1)(n+1)}$
δ_{11}	The self-displacement of hingeless arch	$\int_S (\overline{M_1}^2/EI)ds$	$(1+n)l/EI_o$
δ_{22}		$\int_S \frac{\overline{M_2}^2}{EI} ds + \int_S \frac{\overline{N_2}^2}{EA} ds$	$[2lf^2/EI_o(m-1)]\left\{[(m-2)/2(m-1) - y_s/f](m^2-1)^{1/2}/k + [2(m-1)]^{-1} - (1-n)[((m-2)/2(m-1) - y_s/f)(m^2-1)^{1/2}/k + [4(m-1)]^{-1} - [(m-1)/k^2]((m-3)/4(m-1) - y_s/f)]\right\} + 3l \cos \varphi^{4/3}(1-n^{4/3})/2EA_o(1-n)$
δ_{33}		$\int_S (\overline{M_3}^2/EI)ds$	$(1+3n)l^3/6EI_o$
Δ_{1p}	The load–displacement of hingeless arch	$\int_S (M_1 M_p/EI)ds$	$-(l^2/6EI_o)\left[3(1-x_m/l)^2 - (1-n)(2 - 3x_m/l + {x_m}^3/l^3)\right]$
Δ_{2p}		$\int_S \frac{M_2 M_p}{EI} ds + \int_S \frac{N_2 N_P}{EA} ds$	$-[fl^2/(m-1)EI_o]\{(x_m/kl)(sh(kx_m/l) - shk) + k^{-2}[1 + (1-n)x_m/l](kshk - (kx_m/l)sh(kx_m/l) - chk + ch(kx_m/l)) + [(n-1)/k^3][(k^2+2)shk - (k^2{x_m}^2/l^2 + 2)sh(kx_m/l) - 2k(chk - (x_m/l) ch(kx_m/l))]\} + (l^2/6EI_o)(f/(m-1) + y_s)\left[3(1-x_m/l)^2 - (1-n)(2 - 3x_m/l + {x_m}^3/l^3)\right] - (6.410E-17){x_m}^6 + (2.948E-15){x_m}^5 + (1.637E-13){x_m}^4 - (1.088E-12){x_m}^3 - (4.416E-10){x_m}^2 - (4.020E-10)x_m + 1.619E-7$
Δ_{3p}		$\int_S (M_3 M_p/EI)ds$	$-(l^3/12EI_o)[2(2 - 3x_m/l + {x_m}^3/l^3) - (1-n)(3 - 4x_m/l + {x_m}^4/l^4)]$

Table 2. *Cont.*

Parameter	Significance	Fundamental Mechanical Expression	Practical Analytical Solution
x_1		$-\frac{\int_S (M_1 M_p / EI) ds}{\int_S \left(\overline{M_1}^2 / EI\right) ds}$	$-l\left[3(1-x_m/l)^2-(1-n)(2-3x_m/l+{x_m}^3/l^3)\right]/6(n+1)$
x_2	Redundancy force	$-\frac{\left(\int_S \frac{M_2 M_p}{EI} ds + \int_S \frac{N_2 N_P}{EA} ds\right)}{\left(\int_S \frac{\overline{M_2}^2}{EI} ds + \int_S \frac{\overline{N_2}^2}{EA} ds\right)}$	$\{[fl^2/(m-1)EI_o]\{(x_m/kl)(sh(kx_m/l)-shk)+k^{-2}[1+(1-n)x_m/l](kshk-(kx_m/l)sh(kx_m/l)-chk+ch(kx_m/l))+[(n-1)/k^3][(k^2+2)shk-(k^2{x_m}^2/l^2+2)sh(kx_m/l)-2k(chk-(x_m/l)\ ch(kx_m/l))]\}+(l^2/6EI_o)(f/(m-1)+y_s)\left[3(1-x_m/l)^2-(1-n)(2-3x_m/l+{x_m}^3/l^3)\right]-(6.410E-17){x_m}^6+(2.948E-15){x_m}^5+(1.637E-13){x_m}^4-(1.088E-12){x_m}^3-(4.416E-10){x_m}^2-(4.020E-10)x_m+1.619E-7\}/\{[2lf^2/EI_o(m-1)]\{[(m-2)/2(m-1)-y_s/f](m^2-1)^{1/2}/k+[2(m-1)]^{-1}-(1-n)[((m-2)/2(m-1)-y_s/f)(m^2-1)^{1/2}/k+[4(m-1)]^{-1}-[(m-1)/k^2]((m-3)/4(m-1)-y_s/f)]\}+3l\cos\varphi^{4/3}(1-n^{4/3})/2EA_o(1-n)\}$
x_3		$-\frac{\int_S (M_3 M_p / EI) ds}{\int_S \left(\overline{M_3}^2 / EI\right) ds}$	$\frac{\left[(4-\frac{6x_s}{l}+\frac{2{x_s}^3}{l^3})-(1-n)(3-\frac{4x_s}{l}+\frac{{x_s}^4}{l^4})\right]}{2(1+3n)}$

(Note: When the moving load is in the right half arch, when the x axis is the negative axle in Figure 2, replace x_m of load–displacement Δ_{1P} , Δ_{2P}, and Δ_{3P} with $-x_m$, and Δ_{3P} is minus one time of the corresponding position of the left half span).

Since the constant section is a special case of the variable section, the redundancy force influence line analytical solution of the constant section catenary hingeless arch is a special case of the redundancy force influence line analytical solution of the variable section catenary hingeless arch. When $I = I_0$, the curve integral can be simplified by using the catenary fitting method, i.e., $ds = ch(x/a)dx$. In this paper, the derivation of the redundant influence line analytical solution of the constant section catenary hingeless arch will not be discussed.

2.2. Deflection Influence Line Analytical Solution of Variable Section Hingeless Arch in Non-Damaged Condition

Taking the variable section of the catenary hingeless arch structure as an example, as depicted in Figure 3, based on the redundancy force influence line analytical solution of the variable section catenary hingeless arch derived in Section 2.1, the deflection influence line analytical solution of the variable section catenary hingeless arch structure in non-damaged condition is derived [24,25].

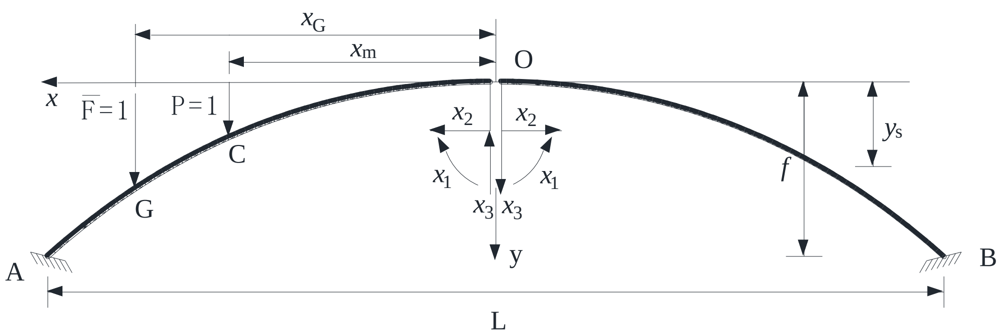

Figure 3. Measurement location G deflection calculation diagram.

There is a dummy unit force $\overline{F} = 1$ at G; when unit force $P = 1$ is applied at C, and redundancy forces x_1, x_2, and x_3 are applied at O, the deflection at G is (Equation (7)):

$$\Delta_G = \begin{cases} -\Delta_{GP} + x_1\Delta_{G1} + x_2\Delta_{G2} + x_3\Delta_{G3} & 0 < x_m < l \\ -\Delta_{GP} + x_1\Delta_{G1} + x_2\Delta_{G2} - x_3\Delta_{G3} & -l < x_m < 0 \end{cases} \tag{7}$$

where Δ_G denotes the deflection of the G point, Δ_{GP} denotes the deflection of moving load at the point, and Δ_{G1}, Δ_{G2} and Δ_{G3} are, respectively, the deflection of redundancy force x_1, x_2, and x_3 at the G point. The mechanical expressions and analytical solutions of Δ_{GP}, Δ_{G1}, Δ_{G2} and Δ_{G3} are as follows (Equations (8)–(11)):

$$\Delta_{GP} = \begin{cases} \int_S \frac{(x_m - x)(x_G - x)}{EI} ds & 0 < x_m < x_G \\ \int_S \frac{(x_m - x)(x_G - x)}{EI} ds & x_G < x_m < l \\ 0 & -l < x_m < 0 \end{cases} \tag{8}$$

$$\Delta_{G1} = \int_S \frac{(x_G - x)}{EI} ds \tag{9}$$

$$\Delta_{G2} = \int_S \frac{(y - y_s)(x_G - x)}{EI} ds + \int_S \frac{\sin\varphi\cos\varphi}{EA} ds \tag{10}$$

$$\Delta_{G3} = \int_S \frac{x(x_G - x)}{EI} ds \tag{11}$$

The corresponding parameters can be derived by substituting Equations (2)–(6) into Equations (8)–(11) for calculation are depicted in Table 3.

Table 3. Analytical solution of deflection influence line of variable section catenary hingeless arch.

Parameter	Significance	Practical Analytical Solution
Δ_{GP}	Deflection at G under moving load P	$\frac{\left[(3n+1)l^2 + (2nx_G - 4nx_m - 2x_m)l + x_G(x_G - 2x_m)(n-1)\right](l - x_G)^2}{12EI_o l}, 0 < x_m < x_G$ $\frac{\left[(3n+1)l^2 + (2nx_m - 4nx_G - 2x_G)l - x_m(2x_G - x_m)(n-1)\right](l - x_G)^2}{12EI_o l}, x_G < x_m < l$ $0, -l < x_m < 0$
Δ_{G1}	Deflection at G under redundancy force x_1	$-\frac{\left[3l^2\left(1 - \frac{x_G}{l}\right)^2 - (1-n)\left(2l^2 - 3x_G l + \frac{x_G{}^3}{l}\right)\right]}{6EI_o}$
Δ_{G2}	Deflection at G under redundancy force x_2	$-\left[fl^2/(m-1)EI_o\right]\{(x_G/kl)(sh(kx_G/l) - shk) + k^{-2}[1 + (1-n)x_G/l]\,(kshk-$ $(kx_G/l)sh(kx_G/l) - chk + ch(kx_G/l)) + \left[(n-1)/k^3\right]$ $\left[(k^2+2)shk - (k^2x_G{}^2/l^2 + 2)\,sh(kx_G/l) - 2k(chk - (x_G/l)ch(kx_G/l))\right]\}+$ $\left(l^2/6EI_o\right)(f/(m-1) + y_s)\left[3(1 - x_G/l)^2 - (1-n)(2 - 3x_G/l + x_G{}^3/l^3)\right]-$ $(6.410 \times 10^{-17})x_G{}^6 + (2.948 \times 10^{-15})x_G{}^5 + (1.637 \times 10^{-13})x_G{}^4 - (1.088 \times 10^{-12})x_G{}^3-$ $(4.416 \times 10^{-10})x_G{}^2 - (4.020 \times 10^{-10})x_G + 1.619 \times 10^{-7}$
Δ_{G3}	Deflection at G under redundancy force x_3	$-\left(l^3/12EI_o\right)[2(2 - 3x_G/l + x_G{}^3/l^3) - (1-n)(3 - 4x_G/l + x_G{}^4/l^4)]$

In summary, by substituting parameters Δ_{GP}, Δ_{G1}, Δ_{G2} and Δ_{G3} in Table 3 and redundancy force influence lines x_1, x_2, and x_3 into (7), the influence line analytical solution of variable section catenary hingeless arch deflection can be obtained. The influence line analytical solution of constant section catenary hingeless arch deflection is derived in the same way as above. When $I = I_0$, the structure section is a constant section. Due to limited space, it will not be repeated here.

3. Deflection Influence Line Analytical Solution of Hingeless Arch in Damaged Condition

3.1. Redundancy Force Influence Line of Constant Section Hingeless Arch in Damaged Condition

The elastic center method is used to simplify the force method equation and the equivalent approximate curve fitting is used to simplify the catenary curve integral. Since the redundancy force influence line is the basis for solving the deflection influence line, therefore, it is the critical to obtain the redundancy force influence line analytical solution of the constant section catenary hingeless arch structure at any section after damage.

By reducing the elastic modulus of the local structure to simulate the damage [26], $E'I$ and $E'A$ represent the degradation of flexural rigidity and tensile rigidity. Taking the hingeless arch of the left span damaged somewhere as an example, a symmetrical basic system is selected by the principle of force method, as depicted in Figure 4.

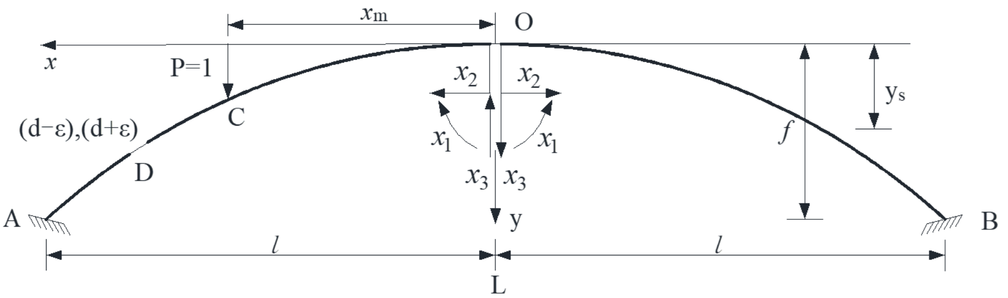

Figure 4. A basic system of the hingeless arch in damaged condition.

As for the constant section catenary hingeless arch, the suspension line fitting was used to simplify the curve integral; that is, $ds = ch(x/a)dx$, its self-displacement values are δ_{11}, δ_{22}, and δ_{33}, load displacement values are Δ_{1P}, Δ_{2P}, and Δ_{3P}, and the analytical expression follows (Equations (12)–(17)):

$$\begin{aligned}\delta_{11} = &(1/EI)\int_0^{d-\varepsilon} ch(x/a)dx + (1/E'I)\int_{d-\varepsilon}^{d+\varepsilon} ch(x/a)dx + (1/EI)\int_{d+\varepsilon}^{l} ch(x/a)dx \\ &+ (1/EI)\int_0^{l} ch(x/a)dx\end{aligned} \tag{12}$$

$$\begin{aligned}\delta_{22} = &(1/EI)\int_0^{d-\varepsilon} (y-y_s)^2 ch(x/a)dx + (1/E'I)\int_{d-\varepsilon}^{d+\varepsilon} (y-y_s)^2 ch(x/a)dx + \\ &(1/EI)\int_{d+\varepsilon}^{l} (y-y_s)^2 ch(x/a)dx + (1/EI)\int_0^{l} (y-y_s)^2 ch(x/a)dx + \\ &(1/EA)\int_0^{d-\varepsilon} \cos\varphi^2 ch(x/a)dx + (1/E'A)\int_{d-\varepsilon}^{d+\varepsilon} \cos\varphi^2 ch(x/a)dx + \\ &(1/EA)\int_{d+\varepsilon}^{l} \cos\varphi^2 ch(x/a)dx + (1/EA)\int_0^{l} \cos\varphi^2 ch(x/a)dx\end{aligned} \tag{13}$$

$$\begin{aligned}\delta_{33} = &(1/EI)\int_0^{d-\varepsilon} x^2 ch(x/a)dx + (1/E'I)\int_{d-\varepsilon}^{d+\varepsilon} x^2 ch(x/a)dx + (1/EI)\int_{d+\varepsilon}^{l} x^2 ch(x/a)dx + \\ &(1/EI)\int_0^{l} x^2 ch(x/a)dx\end{aligned} \tag{14}$$

$$\Delta_{1P} = \begin{cases} (1/EI)\int_{x_m}^{l} (x_m - x)ch(x/\mathrm{a})dx & -l \le x_m \le 0 \\ (1/EI)\int_{x_m}^{d-\varepsilon} (x_m - x)ch(x/\mathrm{a})dx + (1/E'I)\int_{d-\varepsilon}^{d+\varepsilon} (x_m - x)ch(x/\mathrm{a})dx + \\ (1/EI)\int_{d+\varepsilon}^{l} (x_m - x)ch(x/\mathrm{a})dx & 0 \le x_m \le d-\varepsilon \\ (1/E'I)\int_{x_m}^{d+\varepsilon} (x_m - x)ch(x/\mathrm{a})dx + (1/EI)\int_{d+\varepsilon}^{l} (x_m - x)ch(x/\mathrm{a})dx & d-\varepsilon \le x_m \le d+\varepsilon \\ (1/EI)\int_{x_m}^{l} (x_m - x)ch(x/\mathrm{a})dx & d+\varepsilon \le x_m \le l \end{cases} \tag{15}$$

$$\Delta_{2P}=\begin{cases}(1/EI)\int_{x_m}^{l}(x_m-x)(y-y_s)ch(x/a)dx+(1/EA)\int_{x_m}^{l}\cos\varphi\sin\varphi ch(x/a)dx & -l\leq x_m\leq 0\\ (1/EI)\int_{x_m}^{d-\varepsilon}(x_m-x)(y-y_s)ch(x/a)dx+(1/E'I)\int_{d-\varepsilon}^{d+\varepsilon}(x_m-x)(y-y_s)ch(x/a)dx+ & \\ (1/EI)\int_{d+\varepsilon}^{l}(x_m-x)(y-y_s)ch(x/a)dx+(1/EA)\int_{x_m}^{d-\varepsilon}\cos\varphi\sin\varphi ch(x/a)dx+ & 0\leq x_m\leq d-\varepsilon\\ (1/E'A)\int_{d-\varepsilon}^{d+\varepsilon}\cos\varphi\sin\varphi ch(x/a)dx+(1/EA)\int_{d+\varepsilon}^{l}\cos\varphi\sin\varphi ch(x/a)dx & \\ (1/E'I)\int_{x_m}^{d+\varepsilon}(x_m-x)(y-y_s)ch(x/a)dx+(1/EI)\int_{d+\varepsilon}^{l}(x_m-x)(y-y_s)ch(x/a)dx+ & \\ (1/E'A)\int_{x_m}^{d+\varepsilon}\cos\varphi\sin\varphi ch(x/a)dx+(1/EA)\int_{d+\varepsilon}^{l}\cos\varphi\sin\varphi ch(x/a)dx & d-\varepsilon\leq x_m\leq d+\varepsilon\\ (1/EI)\int_{x_m}^{l}(x_m-x)(y-y_s)ch(x/a)dx+(1/EA)\int_{x_m}^{l}\cos\varphi\sin\varphi ch(x/a)dx & d+\varepsilon\leq x_m\leq l\end{cases}\tag{16}$$

$$\Delta_{3P}=\begin{cases}-(1/EI)\int_{x_m}^{l}x(x_m-x)ch(x/a)dx & -l\leq x_m\leq 0\\ (1/EI)\int_{x_m}^{d-\varepsilon}x(x_m-x)ch(x/a)dx+(1/E'I)\int_{d-\varepsilon}^{d+\varepsilon}x(x_m-x)ch(x/a)dx+ & \\ (1/EI)\int_{d+\varepsilon}^{l}x(x_m-x)ch(x/a)dx & 0\leq x_m\leq d-\varepsilon\\ (1/E'I)\int_{x_m}^{d+\varepsilon}x(x_m-x)ch(x/a)dx+(1/EI)\int_{d+\varepsilon}^{l}x(x_m-x)ch(x/a)dx & d-\varepsilon\leq x_m\leq d+\varepsilon\\ (1/EI)\int_{x_m}^{l}x(x_m-x)ch(x/a)dx & d+\varepsilon\leq x_m\leq l\end{cases}\tag{17}$$

The parameters of self-displacement and load–displacement are introduced into the expression of redundancy force influence line, $x_1=-\Delta_{1P}/\delta_{11}$, $x_2=-\Delta_{2P}/\delta_{22}$ and $x_3=-\Delta_{3P}/\delta_{33}$. The redundancy force influence line analytical solution of any section after the damage of the catenary hingeless arch can be obtained.

3.2. Deflection Influence Line Analytical Solution of Constant Section Hingeless Arch in Damaged Condition

Taking the left half span as the research object, according to the deflection calculation diagram of measuring location G under the damage condition in Figure 5, the deflection influence line of location G is solved by the principle of virtual work:

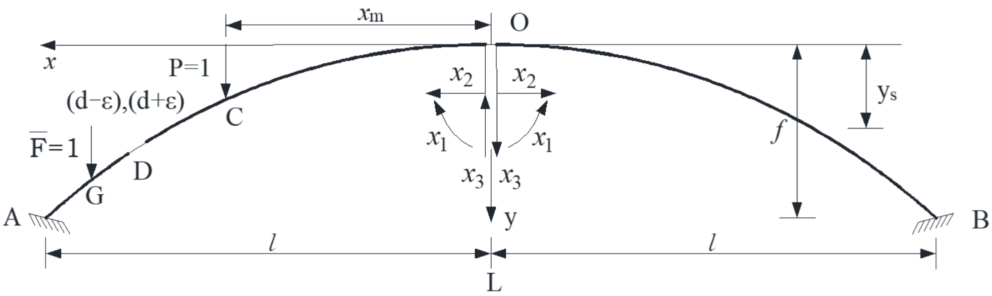

Figure 5. Measurement location G deflection in damaged condition calculation diagram.

There is a dummy unit force $\overline{F}=1$ at G, when unit force $P=1$ is applied at C and redundancy force x_1, x_2 and x_3 are applied at O, the deflection expression at G is Formula (7), and the cross-section is in the form of a constant section, and catenary fitting is selected.

According to the location of the moving force, Δ_{GP}, Δ_{G1}, Δ_{G2}, and Δ_{G3} can be divided into the following states (Equations (18)–(21)):

$$\Delta_{GP}=\begin{cases}0 & -l<x_m<0\\ \int_{x_G}^{l}\frac{(x_m-x)(x_G-x)}{EI}\cosh\left(\frac{x}{a}\right)dx & 0<x_m<x_G\\ \int_{x_m}^{l}\frac{(x_m-x)(x_G-x)}{EI}\cosh\left(\frac{x}{a}\right)dx & x_G<x_m<l\end{cases}\tag{18}$$

$$\Delta_{G1}=\int_{x_G}^{l}\frac{x_G-x}{EI}\cosh\left(\frac{x}{a}\right)dx\tag{19}$$

$$\Delta_{G2} = \int_{x_G}^{l} \frac{(x_G - x)(y - y_s)}{EI} \cosh\left(\frac{x}{a}\right) dx \tag{20}$$

$$\Delta_{G3} = \int_{x_G}^{l} \frac{(x_G - x)x}{EI} \cosh\left(\frac{x}{a}\right) dx \tag{21}$$

The analytical solution of the deflection generated by each force at G is depicted in Table 4.

Table 4. Analytical solution of deflection influence line.

Parameter	Significance	Practical Analytical Solution
Δ_{GP}	Deflection at G under moving load P	$0, -l < x_m < 0$ $-\frac{\left[a^2\left((-2x_m + 4l - 2x_G)\cosh\left(\frac{l}{a}\right) + (x_m - 2a - x_G)e^{-\frac{x_G}{a}} + (x_m + 2a - x_G)e^{\frac{x_G}{a}}\right)\right]}{2EI} - \frac{\left[a\sin\left(\frac{l}{a}\right)\left(-4a^2 + (2l - 2x_G)(-l + x_m)\right)\right]}{2EI}, 0 < x_m < x_G$ $-\frac{\left[a^2\left((-2x_m - 4l + 2x_G)\cosh\left(\frac{l}{a}\right) + (x_m + 2a - x_G)e^{-\frac{x_m}{a}} + (x_m - 2a - x_G)e^{\frac{x_m}{a}}\right)\right]}{2EI} - \frac{\left[a\sin\left(\frac{l}{a}\right)\left(-4a^2 + (2l - 2x_G)(-l + x_m)\right)\right]}{2EI}, x_G < x_m < 0$
Δ_{G1}	Deflection at G under redundancy force x_1	$-\frac{a\left[(2l - 2x_G)\sin\left(\frac{l}{a}\right) - (1 - n)\left(2l^2 - 3x_B l + \frac{{x_B}^3}{l}\right)\right]}{2EI}$
Δ_{G2}	Deflection at G under redundancy force x_2	$\frac{ae^{\frac{-k(l+x_G)a - x_G l}{la}}}{4EI\left(4l^2 - 4a^2(d+\varepsilon)^2\right)^2}\left[-\left(2l - 4a^2(d+\varepsilon)^2\right)^2(2l + 2a - 2x_G)(c + y_s)e^{\frac{-l^2 + (a(d+\varepsilon)+x_G)l + x_G(d+\varepsilon)a}{la}} + \right.$ $\left(4l^2 + 2(2a - 2(d+\varepsilon)a - 2x_G)l + 4x_G(d+\varepsilon)a\right)(2a(d+\varepsilon) + 2l)^2 lCe^{\frac{-l^2 + (2a(d+\varepsilon)+x_G)l + x_G(d+\varepsilon)a}{la}} -$ $\left(4l^2 + 2(2(d+\varepsilon)a - 2a - 2x_G)l - 4x_G(d+\varepsilon)a\right)(-2a(d+\varepsilon) + 2l)^2 lCe^{\frac{l^2(2a(d+\varepsilon)+x_G)l + x_G(d+\varepsilon)a}{la}} +$ $\left(4l^2 + (2(d+\varepsilon)a + 2a - 2x_G)2l - 4x_G(d+\varepsilon)a\right)(-2a(d+\varepsilon) + 2l)^2 lCe^{\frac{-x_G(d+\varepsilon)a + l^2 - x_G l}{la}} -$ $\left(4l^2 + (-2(d+\varepsilon)a - 2a - 2x_G)2l + 4x_G(d+\varepsilon)a\right)(2a(d+\varepsilon) + 2l)^2 lCe^{\frac{x_G(d+\varepsilon)a + l^2 + x_G l}{la}} +$ $2a\left(4l^2 - 4a^2(d+\varepsilon)^2\right)^2(C + y_s)e^{\frac{(d+\varepsilon)(l+x_G)a + 2x_G l}{la}} - 4l^2Ca(-2a(d+\varepsilon) + 2l)^2 e^{\frac{(d+\varepsilon)(l+2x_G)a + 2x_G l}{la}} +$ $\left(4l^2 - 4a^2(d+\varepsilon)^2\right)^2(2l - 2a - 2x_G)(C + y_s)e^{\frac{(l+x_G)(a(d+\varepsilon)+l)}{la}} - 4al^2C\left[4l^2C(2a(d+\varepsilon) + 2l)^2 e^{\frac{a(d+\varepsilon)+2x_G}{a}} - \right.$ $\left.\left.2\left(4l^2 - 4a^2(d+\varepsilon)^2\right)^2(C + y_s)e^{\frac{(d+\varepsilon)(l+x_G)}{l}} + \left((2a(d+\varepsilon) + 2l)^2 e^{\frac{(d+\varepsilon)(l+2x_G)}{l}} + e^{(d+\varepsilon)}(2l - 2a(d+\varepsilon))^2\right)\right]\right]$
Δ_{G3}	Deflection at G under redundancy force x_3	$-\frac{a\left[2a^2 + l(l - x_G)\right]\sinh\left(\frac{l}{a}\right)}{EI} +$ $\frac{a^2\left[(2l - x_G)\cosh\left(\frac{l}{a}\right) + \left(-a - \frac{x_G}{2}\right)e^{-\frac{x_G}{a}} + e^{\frac{x_G}{a}}\left(a - \frac{x_G}{2}\right)\right]}{EI}$

In a similar way, the parameters in Table 4 and the analytical solutions x_1, x_2 and x_3 of the redundancy force influence line of any section after damage are substituted into Equation (7) to obtain the deflection influence line analytical solution of the hingeless arch after damage.

4. Establishment of Damage Identification Index DILDC

The analytical solutions of the redundancy forces x_1, x_2, x_3 and Δ_{GP}, Δ_{G1}, Δ_{G2} and Δ_{G3} of the arch rib damaged structure are introduced into Equation (7), and the deflection influence line $\Delta_G{}'$ after damage is obtained. Subtract the damaged deflection influence line $\Delta_G{}'$ with the non-damaged deflection influence line Δ_G, and take the second derivative of this calculation result. Therefore, the identification index DILDC of the curvature damage of deflection influence line difference is proposed.

To simplify the index expression, let $C = f/(m-1)$. The calculation and analysis of the second derivative $\Delta_{2P_{S1}}''$ and Δ_{2P2}'' of the displacement position x_m by the load–displacement in the direction of redundancy force x_2 in the damage region are as follows:

$$\begin{aligned}\Delta_{2P_{S1}}'' &= \tfrac{1}{E'I}\int_{x_m}^{d+\varepsilon}(x_m-x)(y-y_s)ch\tfrac{x}{a}dx \\ &= \tfrac{1}{E'I}\left(-Ce^{-\frac{(-ak+l)x_m}{la}}/4-Ce^{-\frac{(ak+l)x_m}{la}}/4-Ce^{\frac{(-ak+l)x_m}{la}}/4-Ce^{\frac{(ak+l)x_m}{la}}/4+(e^{\frac{x_m}{a}}+e^{-\frac{x_m}{a}})(C+y_s)/2\right)\end{aligned}$$

$$\begin{aligned}\Delta_{2P_{S2}}'' &= \frac{1}{E'A}\int_{x_m}^{d+\varepsilon}\cos\varphi\sin\varphi ch\frac{x}{a}dx \\ &= \frac{-kf(m-1)}{aE'A\left[(m-1)^2l^2+k^2f^2sh\left(\frac{kx_m}{l}\right)^2\right]^2}\left[sh\left(\frac{kx_m}{l}\right)^3 sh\left(\frac{x_m}{a}\right)f^2k^2l-\right. \\ &\quad sh\left(\frac{kx_m}{l}\right)^2 ch\left(\frac{x_m}{a}\right)ch\left(\frac{kx_m}{l}\right)k^3f^2a+(m-1)^2l^3sh\left(\frac{x_m}{a}\right)sh\left(\frac{kx_m}{l}\right)+ \\ &\quad \left. akl^2(m-1)^2ch\left(\frac{x_m}{a}\right)ch\left(\frac{kx_m}{l}\right)\right]\end{aligned}$$

The G deflection influence line difference curvature $(\Delta_G-\Delta_G{}')''$ of the arch rib section before and after damage can be divided into the following five scenarios (Equations (22)–(26)):

When $-l \le x_m \le 0$

$$(\Delta_G-\Delta_G{}')''=0 \tag{22}$$

When $0 \le x_m \le d-\varepsilon$

$$(\Delta_G-\Delta_G{}')''=0 \tag{23}$$

When $d-\varepsilon \le x_m \le d+\varepsilon$

$$\begin{aligned}(\Delta_G-\Delta_G{}')'' &= \frac{\left(e^{\frac{x_m}{a}}+e^{-\frac{x_m}{a}}\right)}{2}\left(\frac{x_m\Delta_{G3}}{EI\delta_{33}}-\frac{x_m\Delta_{G3}}{E'I\delta_{33}}+\frac{\Delta_{G1}}{EI\delta_{11}}-\frac{\Delta_{G1}}{E'I\delta_{11}}\right)+ \\ &\quad \left(\frac{\Delta_{G2}}{E'I\delta_{22}}-\frac{\Delta_{G2}}{EI\delta_{22}}\right)\Delta_{2P_{S1}}''E'I+\left(\frac{\Delta_{G2}}{E'A\delta_{22}}-\frac{\Delta_{G2}}{EA\delta_{22}}\right)\Delta_{2P_{S2}}''E'A\end{aligned} \tag{24}$$

When $d+\varepsilon \le x_m \le x_G$

$$(\Delta_G-\Delta_G{}')''=0 \tag{25}$$

When $x_G \le x_m \le l$

$$(\Delta_G-\Delta_G{}')''=0 \tag{26}$$

According to Equations (22)–(26), when the moving load is located in the non-damaged sector, the curvature $(\Delta_G-\Delta_G{}')''$ pertaining to the deflection influence line difference of arch rib section G is zero, whereas when the moving load is located in the non-damaged sector, and the curvature $(\Delta_G-\Delta_G{}')''$ of the deflection influence line difference is a value that is not zero, it results in sudden change. Subsequently, the damage location can be identified and the damage extent can be quantitatively judged according to the magnitude of the sudden change.

5. Example Analysis

5.1. Accuracy Analysis of the Deflection Influence Line Analytical Solution

To identify the analytical accuracy of the deflection influence line derived in Section 2.2, a finite element model was established by taking four variable section catenary hingeless arches as examples; the calculated results of the derived deflection influence line were compared, and the relative errors of the analytical solution and the finite element numerical solution were compared. The span of the four arches is 40 m, and the rise–span ratios are

1/2, 1/3, 1/5, and 1/7, as depicted in Figure 6. The width of the arch rib section is 1 m, and the height of the mid-span arch section is 1 m. The section height changes according to the Ritter formula (Equations (4)–(6)), the elastic modulus of the material is 3.45×10^7 kN/m^2, the arch axis coefficient m is 1.988, and the arch thickness change coefficient n is 0.4. The deflection influence lines of $L/2$ and $L/4$ sections for formula analysis and finite element calculation in this paper are illustrated in Figures 7–10, and the numerical results of typical sections are depicted in Table 5.

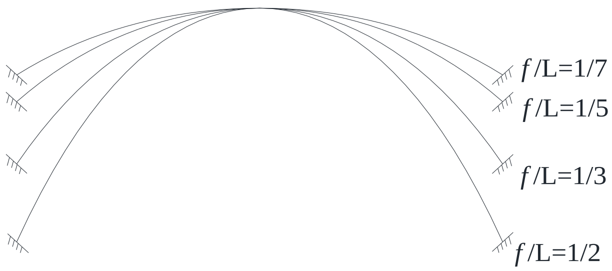

Figure 6. Four specific rise–span ratio arch axes.

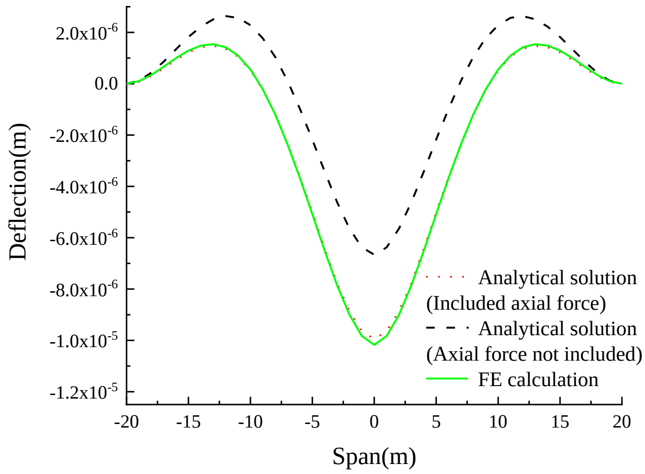

Figure 7. Section L/2.

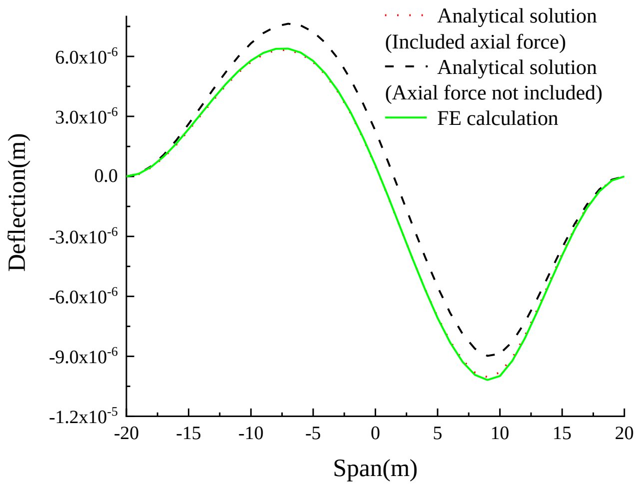

Figure 8. Section L/4.

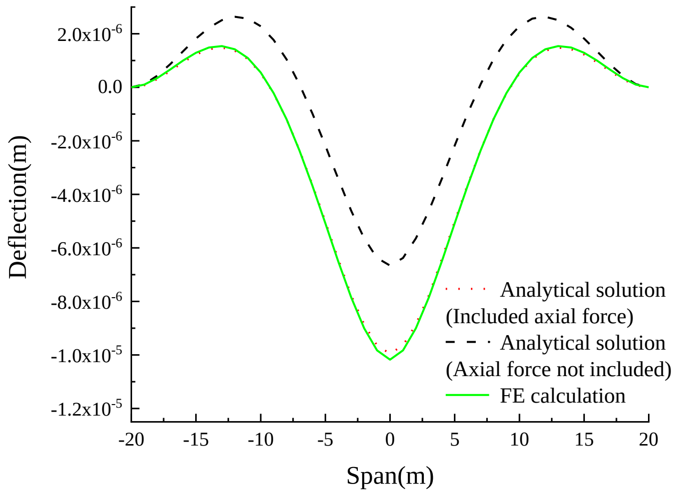

Figure 9. Section L/2.

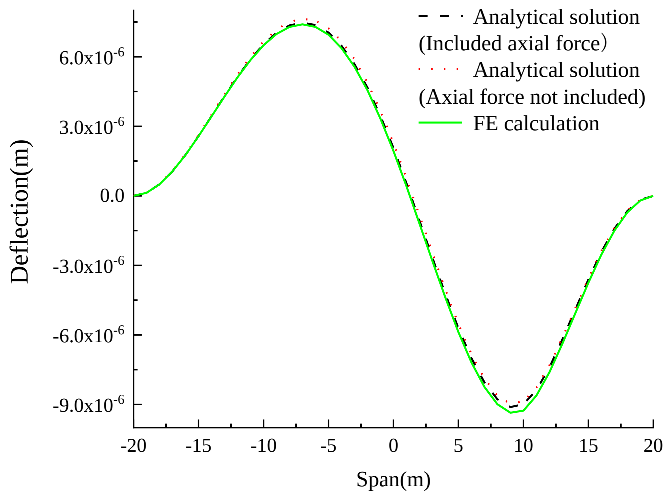

Figure 10. Section L/4.

The comparison between the analytical solutions of different typical sections in example 1 (unit: m) and the FE numerical calculation are depicted in Figures 7 and 8.

The comparison between the analytical solutions of different typical sections in example 4 (unit: m) and the FE numerical calculation are depicted in Figures 9 and 10.

From the analysis of Table 5, Figures 7–10, it can be seen that for arch axes with different rise–span ratios, when the axial force is considered, the deviation between the deflection influence lines analytical solutions of the four kinds of variable cross-section catenary hingeless arch in the calculation examples, and the result of the finite element calculation is less than 6%.

However, when the axial force is not considered, the calculation deviation pertaining to the deflection influence line analytical solution of the variable section catenary hingeless arch of 1/2 and 1/3 rise–span ratios can be controlled within 20%. However, the analytical calculation deviation of the measuring location $L/2$ of the 1/5 and 1/7 rise–span ratios deflection influence line is larger than 20%, and the maximum calculation deviation is greater than 300%.

For the same rise–span ratios, the analytical deviation of the influence line at measuring location $L/4$ is generally smaller than that at measuring location $L/2$, and the influence of axial force at measuring location $L/4$ is less than that at measuring location $L/2$.

Table 5. Typical cross-section value comparison table of calculation examples.

Load Position \ Deflection of Section			L/2 Analytical Solution/m	L/2 Numerical Solution/m	L/2 Relative Error/%	L/4 Analytical Solution/m	L/4 Numerical Solution/m	L/4 Relative Error/%
Example 1 (rise–span ratio 1/7)	Axial force	$-L/4$	5.233×10^{-7}	5.540×10^{-7}	5.541	5.723×10^{-6}	5.795×10^{-6}	1.242
		$L/2$	-9.951×10^{-6}	-1.017×10^{-5}	2.153	5.233×10^{-7}	5.540×10^{-7}	5.541
		$L/4$	5.233×10^{-7}	5.540×10^{-7}	5.541	-9.806×10^{-6}	-9.988×10^{-6}	1.822
	Axial force not included	$-L/4$	2.279×10^{-6}	5.540×10^{-7}	311.460	6.660×10^{-6}	5.795×10^{-6}	12.987
		$L/2$	-6.660×10^{-6}	-1.017×10^{-5}	34.540	2.279×10^{-6}	5.540×10^{-7}	311.460
		$L/4$	2.279×10^{-6}	5.540×10^{-7}	311.460	8.870×10^{-6}	-9.988×10^{-6}	11.193
Example 2 (rise–span ratio 1/5)	Axial force	$-L/4$	1.296×10^{-6}	1.295×10^{-6}	0.077	6.131×10^{-6}	6.169×10^{-6}	0.615
		$L/2$	-8.486×10^{-6}	-8.720×10^{-6}	2.683	1.296×10^{-6}	1.295×10^{-6}	0.077
		$L/4$	1.296×10^{-6}	1.295×10^{-6}	0.077	-9.399×10^{-7}	-9.590×10^{-6}	1.991
	Axial force not included	$-L/4$	2.279×10^{-6}	1.295×10^{-6}	43.176	6.660×10^{-6}	6.169×10^{-6}	7.372
		$L/2$	-6.660×10^{-6}	-8.720×10^{-6}	23.623	2.279×10^{-6}	1.295×10^{-6}	43.176
		$L/4$	2.279×10^{-6}	1.295×10^{-6}	43.176	-8.870×10^{-6}	-9.590×10^{-6}	7.507
Example 3 (rise–span ratio 1/3)	Axial force	$-L/4$	1.861×10^{-6}	1.795×10^{-6}	3.546	6.431×10^{-6}	6.417×10^{-6}	0.217
		$L/2$	-7.423×10^{-6}	-7.700×10^{-6}	3.597	1.861×10^{-6}	1.795×10^{-6}	3.546
		$L/4$	1.861×10^{-6}	1.795×10^{-6}	3.546	-9.099×10^{-6}	-9.322×10^{-6}	2.392
	Axial force not included	$-L/4$	2.279×10^{-6}	1.795×10^{-6}	21.237	6.660×10^{-6}	6.417×10^{-6}	3.648
		$L/2$	-6.660×10^{-6}	-7.700×10^{-6}	13.506	2.279×10^{-6}	1.795×10^{-6}	21.237
		$L/4$	2.279×10^{-6}	1.795×10^{-6}	21.237	-8.870×10^{-6}	-9.322×10^{-6}	4.848
Example 4 (rise–span ratio 1/2)	Axial force	$-L/4$	2.059×10^{-6}	1.936×10^{-6}	5.973	6.538×10^{-8}	6.495×10^{-6}	0.657
		$L/2$	-7.055×10^{-6}	-7.373×10^{-6}	4.313	2.059×10^{-6}	1.936×10^{-6}	5.973
		$L/4$	2.059×10^{-6}	1.936×10^{-6}	5.973	-8.991×10^{-6}	-9.265×10^{-6}	2.957
	Axial force not included	$-L/4$	2.279×10^{-6}	1.936×10^{-6}	15.050	6.660×10^{-6}	6.495×10^{-6}	2.477
		$L/2$	-6.660×10^{-6}	-7.373×10^{-6}	9.670	2.279×10^{-6}	1.936×10^{-6}	15.050
		$L/4$	2.279×10^{-6}	1.936×10^{-6}	15.050	-8.870×10^{-6}	-9.265×10^{-6}	4.263

5.2. Arch Rib Structure Example Verification

The hingeless single arch structure finite element model is established as a simplified model of the bridge arch rib. The span is L = 50.934 m, the material is C50 concrete, and a rectangular section of 1 m × 1.3 m is utilized, as depicted in Figure 11.

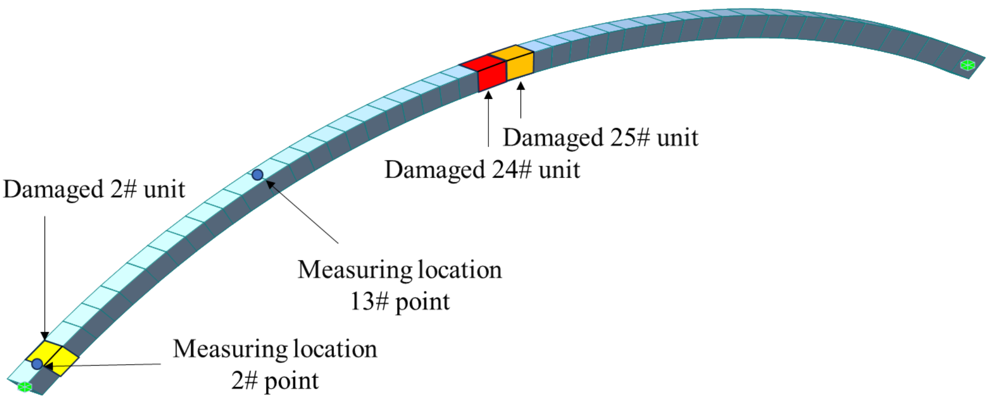

Figure 11. Hingeless single arch structure finite element model.

In the process of example verification, the local damage is simulated by reducing the element elastic modulus. The section size and the mass of the damaged element remain unchanged. The damage extent is defined by the percentage decline in the elastic modulus.

The hingeless single arch model is divided into 48 beam elements. The quasi-static moving force is applied as the influence line loading method, and the length of the loading element is 1.061 m with a total of 49 moving loading steps. Damage conditions 1–5 are illustrated in Table 6. The noise introduction method is illustrated in Equations (27) and (28) [27,28].

$$\Delta_i{}^N = \Delta_i \cdot [1 + \mu \cdot RAND(-1, 1)] \tag{27}$$

$$\Delta^N(x') = \left[\Delta_1{}^N \cdots \Delta_i{}^N \cdots \Delta_n{}^N\right] \tag{28}$$

where Δ_i denotes the deflection data extracted from the measurement location under the i loading step, $\Delta_i{}^N$ denotes the deflection data containing noise at the i loading step, $RAND(-1, 1)$ denotes a random number that follows a standard normal distribution, μ denotes the noise extent level, and superscript N indicates that the quantity value has included the introduced noise information. The damage index is constructed using the deflection data containing noise to verify the noise immunity of the proposed method.

The moving load is applied to the single hingeless arch structure, and the DILDC curve of the corresponding measuring location in Table 6 is extracted. The damage identification results of the arch rib structure identification curve are drawn as illustrated in Figures 12–15 (unit: mm). The damage identification results in the noise condition are drawn as illustrated in Figure 16 (unit: mm).

Table 6. Damage condition of the arch structure.

Damage Condition	Damage Unit	Damage Extent	Measuring Location (Point)	Result of Identify
Work condition 1	24#	5%, 10%, 20%, 40%	13#	Figure 12
Work condition 2	24#	5%, 10%, 20%, 40%	2#	Figure 13
Work condition 3	2#, 24#	10%	13#	Figure 14
Work condition 4	Between Unit 24# and unit 25#	Mid-span plastic hinge	13#	Figure 15
Work condition 5	24#	40% (Noise extent 1%, 3%, 5%)	13#	Figure 16

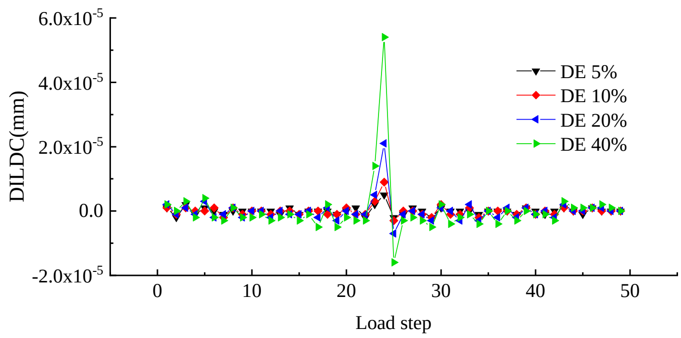

Figure 12. Work condition 1.

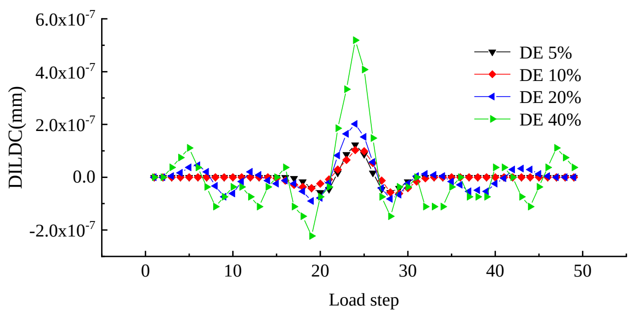

Figure 13. Work condition 2.

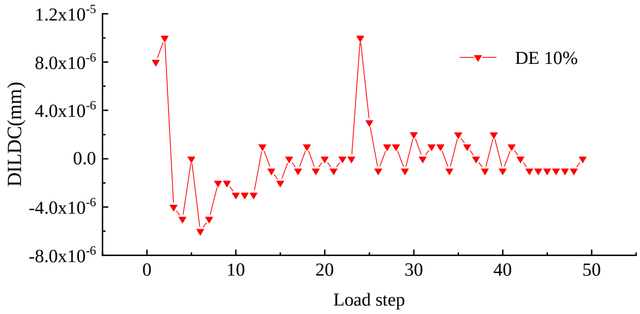

Figure 14. Work condition 3.

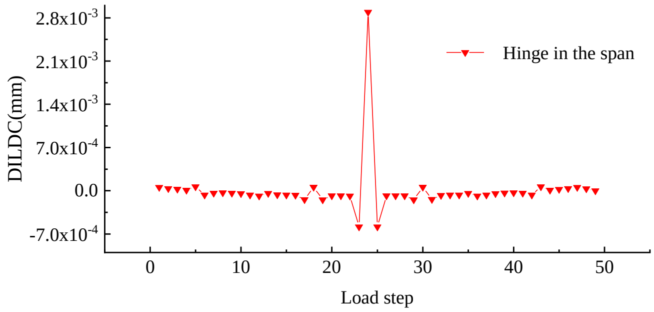

Figure 15. Work condition 4.

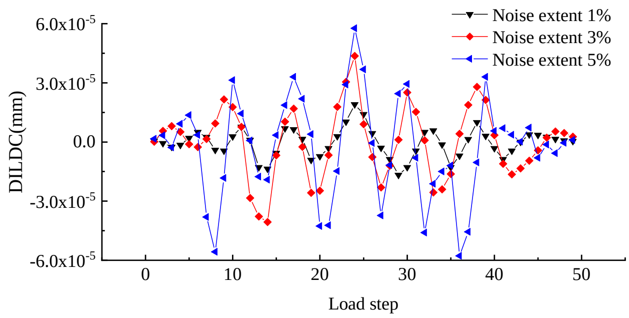

Figure 16. Work condition 4.

To better explore the effect of measuring location and unit damage extent on DILDC damage identification, the DILDC index curves of 40% damage and 5% damage extent in Work condition 1 and Work condition 2 were compared, respectively, as illustrated in Figures 17–20 (unit: mm).

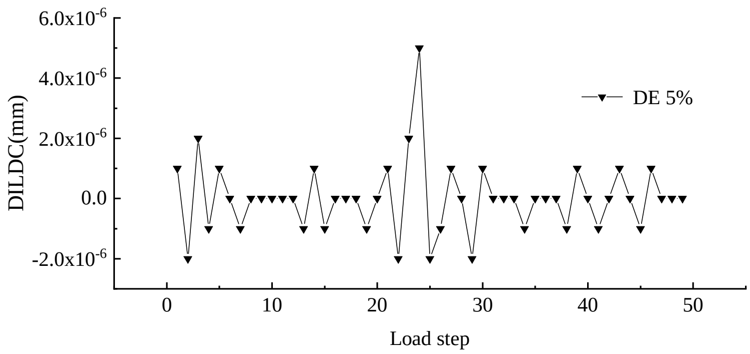

Figure 17. Work condition 1.

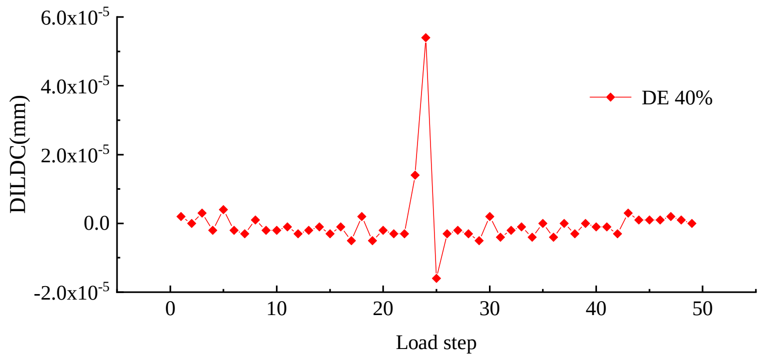

Figure 18. Work condition 1.

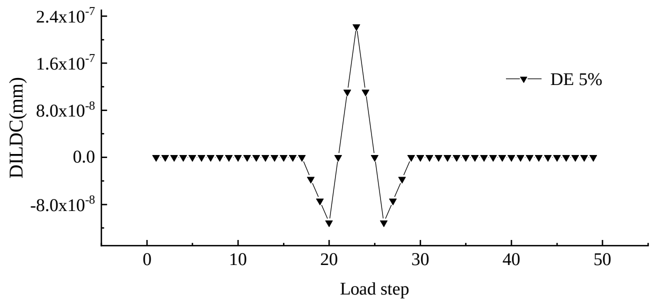

Figure 19. Work condition 2.

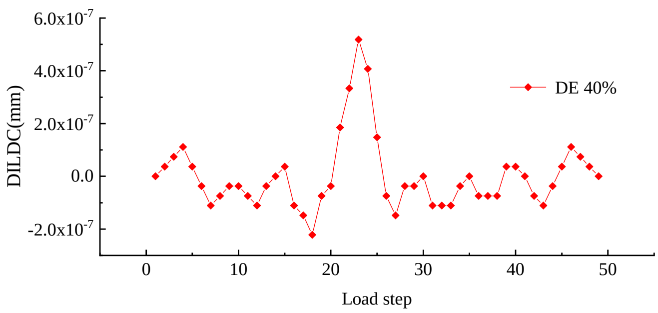

Figure 20. Work condition 2.

Through the analysis of Figures 12–20, the following can be observed:

(1) The DILDC index identification method exhibits a satisfactory identification effect on both the single location damage and multiple location damage of hingeless arch structures, and it can accurately identify the damage location.

(2) According to conditions 1 and 2, the amplitude height of the curve is proportional to the damage extent at the same measuring location. Compared with Work conditions 1 and 2, the amplitude height of the quarter-span DILDC index curve at the measuring location is greater than that at the arch foot, and the damage identification effect of the measuring location at the quarter-span is better than that at the arch foot. Therefore, the closer the measuring location is to the damage location, the better the identification effect will be. It is worth noting that the damage identification effect of DILDC on unit damage at 40% is better than that of unit damage at 5% under the condition of one-quarter measuring location, and the situation is the opposite when the measuring location is located at the arch foot.

(3) Figure 16 indicates that when the damage extent is 40% and the noise extents are 1%, 3% and 5%, the damage location can still be effectively identified, and the noise immunity of DILDC is good.

The analytical solution theoretical value derived in Section 4 is compared with the Work condition of 40% damage extent in Work condition 1.

When the moving load is located at the damage location at the i end of unit 24, the basic data of the bridge is put into Equation (29):

$$\begin{aligned}(\Delta_G - \Delta_G{}')'' &= \frac{\left(e^{\frac{x_m}{a}} + e^{-\frac{x_m}{a}}\right)}{2}\left(\frac{x_m \Delta_{G3}}{EI\delta_{33}} - \frac{x_m \Delta_{G3}}{E'I\delta_{33}} + \frac{\Delta_{G1}}{EI\delta_{11}} - \frac{\Delta_{G1}}{E'I\delta_{11}}\right) + \\ &\quad \left(\frac{\Delta_{G2}}{E'I\delta_{22}} - \frac{\Delta_{G2}}{EI\delta_{22}}\right)\Delta_{2P_{S1}}{}'' E'I + \left(\frac{\Delta_{G2}}{E'A\delta_{22}} - \frac{\Delta_{G2}}{EA\delta_{22}}\right)\Delta_{2P_{S2}}{}'' E'A \\ &= 4.911 \times 10^{-5}\end{aligned} \tag{29}$$

The deviation between the obtained values and the finite element results is 9.1%, which is analyzed as the deviation caused by curve fitting, and the deviation satisfies the needs of practical engineering calculation and application.

In order to explore the relationship between damage extent and DILDC amplitude and to invert the damage extent, DILDC amplitudes under severe damage extent were taken in Work condition 1. The relationship between damage extent and amplitude is illustrated in Table 7 and Figure 21.

Table 7. Maximum value of DILDC in different damage extent conditions.

Damage Extent x	**0%**	**20%**	**40%**	**60%**	**80%**	**90%**	**99.9%**
Amplitude $S(x)_{max}$	0	2.10×10^{-5}	5.40×10^{-5}	1.21×10^{-4}	2.93×10^{-4}	5.67×10^{-4}	2.05×10^{-2}

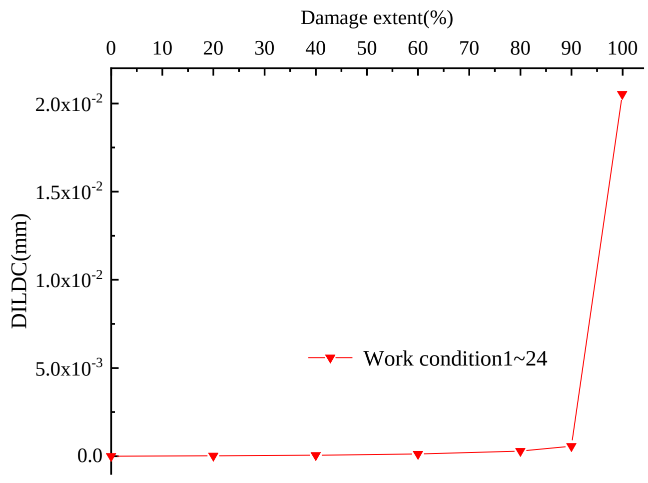

Figure 21. Relation between damage extent and DILDC.

As shown in Figure 21, when the damage extent is less than 90%, the amplitude of DILDC changes gently, and the increase in the damage extent of elements has little impact on the structural rigidity characteristics and has a certain safety reserve. However, with the increase in the damage extent, the amplitude of DILDC changes sharply and long, and the damage extent has a greater impact on the structural rigidity characteristics, and the structural safety performance becomes low. This is consistent with the actual structural damage change law.

The DILDC amplitude in Figure 21 is fitted with the damage extent, and the fitting results are shown in Equation (30), where the subscript of $DILDC_{a\text{-}b}$ amplitude a-b represents the amplitude of unit b in Work condition a.

$$DILDC_{1\text{-}24}(x) = 1.2372x^5 - 2.7658x^4 + 2.1637x^3 - 0.687x^2 + 0.0725x - 0.00004 \tag{30}$$

The goodness of fit was analyzed, and the determination coefficient R = 0.981 indicated that the fitting effect was good. Taking the arch rib structure as an example, the damage extent could be directly obtained by substituting the DILDC amplitude into Equation (30) for the determined work conditions.

In Work condition 4, the rigid joint is weakened into a hinge to simulate the plastic hinge in the actual structure. The DILDC value of the damage location is substituted into Equation (30), and the calculated damage extent x is 90.95%, which is close to 100.00% in the case of complete damage.

5.3. Example Verification of Deck Box-Type Arch Bridge

The model of a single-span concrete deck box arch bridge is established, and the practicability of the damage identification method is verified. The quasi-static moving force is applied as the influence line loading method, and the length of the deck is 120 m with a total of 29 moving loading steps. The span of the arch bridge model is 116 m, the main arch ring is made of C40 concrete, and the elastic modulus is 32.5 Gpa. The model comprises 82 units and 96 nodes. The finite element model and component dimensions of the deck box-type arch bridge are illustrated in Figures 22 and 23.

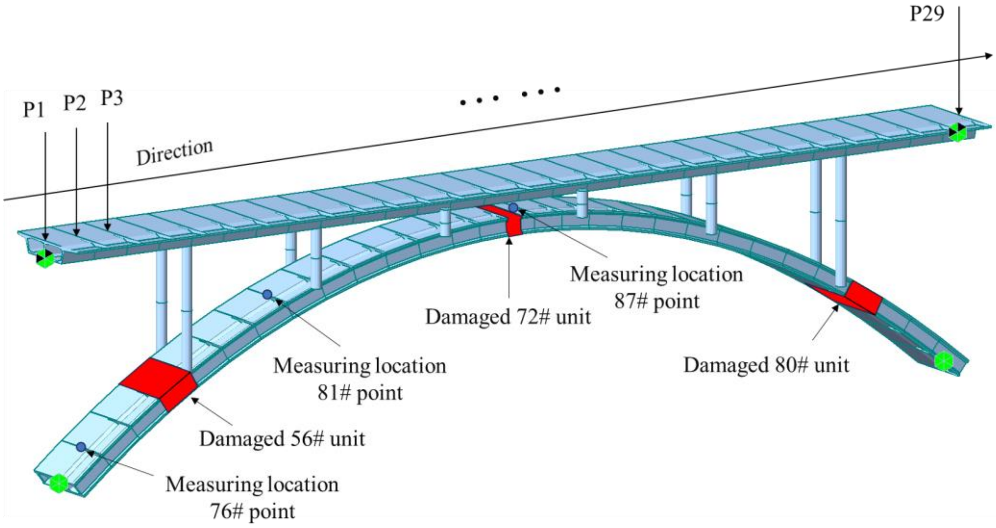

Figure 22. Deck box-type arch bridge finite element.

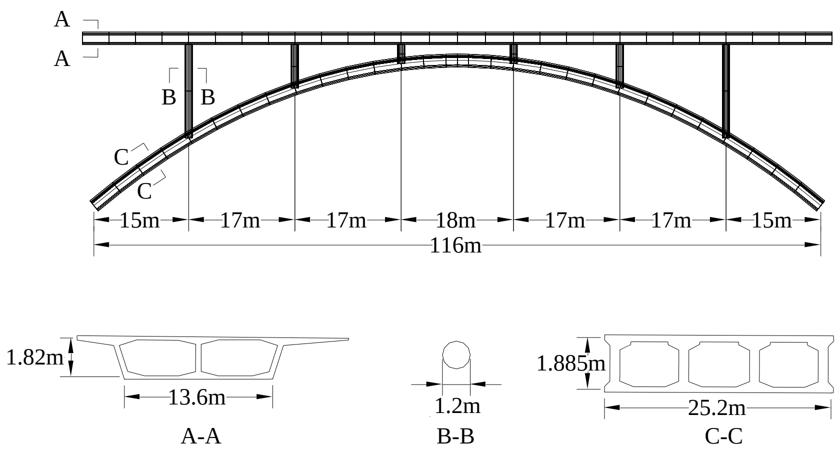

Figure 23. Component dimensions of deck box-type arch bridge.

Next, we explored the damage identification effect of DILDC on the deck-type box arch bridge. According to the damage of the main arch ring of the main load-bearing component in practical engineering, five damage conditions are established, as illustrated in Table 8 and Figure 24.

Table 8. Damage condition of deck box-type arch bridge.

Damage Condition	Damage Unit	Damage Extent	Measuring Location (Point)	Identify the Result
Work condition 1	Main arch ring top 72#	5%, 10%, 20%, 40%	81#	Figure 25
Work condition 2	Main arch ring top 72#	5%, 10%, 20%, 40%	76#	Figure 26
Work condition 3	Main arch ring top 72#	5%, 10%, 20%, 40%	87#	Figure 27
Work condition 4	Main arch ring 56, 80#	5%	81#	Figure 28
Work condition 5	Main arch ring top 72#	5% (Noise intensity 1%, 3%, 5%)	81#	Figure 29

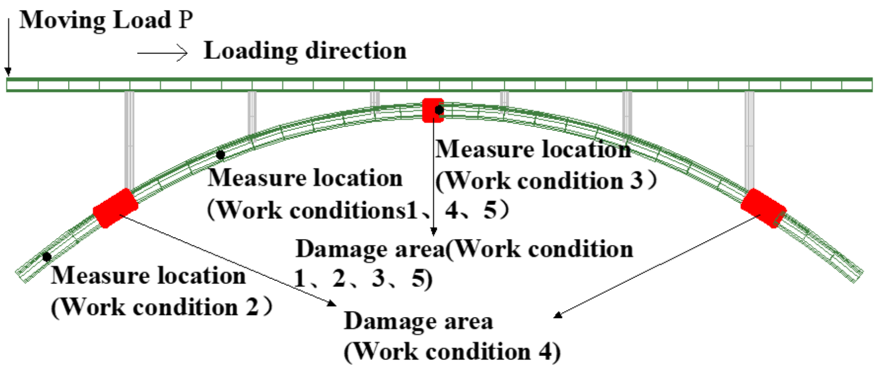

Figure 24. Main arch span damage condition and arrangement measuring location.

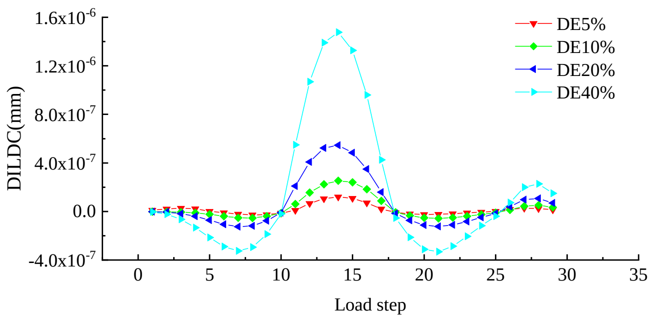

Figure 25. Work condition 1.

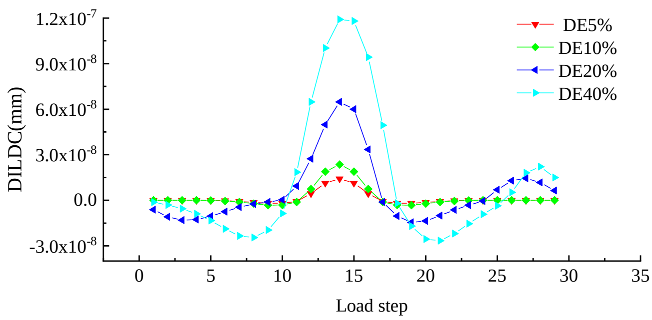

Figure 26. Work condition 2.

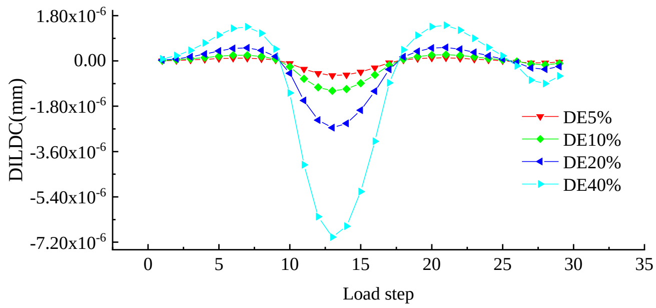

Figure 27. Work condition 3.

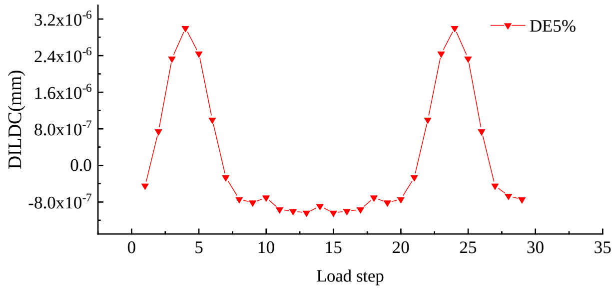

Figure 28. Work condition 4.

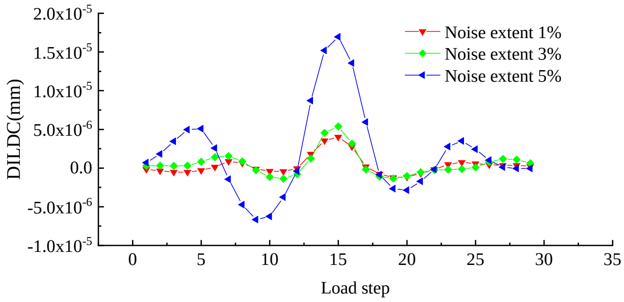

Figure 29. Work condition 5.

The damage identification results of the arch ring structure identification curve are drawn as illustrated in Figures 25–28 (unit: mm). And the damage identification results in noise condition are drawn as illustrated in Figure 29 (unit: mm).

According to the analysis of Figures 25–28, for the deck box-type arch bridge, due to the limited number of actual force-transmitting structure columns and the unbalanced force on the main arch ring, the identification effect is not good. Therefore, the DILDC index obtained is processed by sliding average filtering. The numerical examples show that the filtered DILDC index has a good effect on the damage identification of the main arch ring structure, and the amplitude of the DILDC index curve changes with the change in damage extent. The higher the damage extent, the higher the amplitude. According to Work conditions 1, 2 and 3, the amplitude of the curve decreases with the position of the deflection measuring location from mid-span, one-quarter and arch foot. According to Work condition 4, it can be seen that the multi-point damage of the structure still has a good identification effect.

Figure 29 indicates that the DILDC index after filtering and noise reduction also exhibits a satisfactory noise immunity to 5% low damage extent structures.

6. Practical Process of Damage Identification for Hingeless Arch Bridges

In order to solve the problem that it is difficult to apply single-axis concentrated load in a beam bridge influence line test, a three-step loading scheme based on moving load reduction is proposed to diagnose beam bridge damage quickly when traffic is interrupted for a short time [29,30], as illustrated in Figure 30.

(1) Select two two-axle loading vehicles with the same wheelbase and different front-to-rear axle load ratios. The front, back and axle of each vehicle can be simplified to the same relative position, while the value of the concentration force is different. It should be noted that the actual loading efficiency should consider both the effective stimulation of the structure and the potential damage condition of the bridge. Due to the limitation of the length of this study, we will not conduct in-depth research here.

(2) Two vehicles are used to carry out quasi-static influence line loading on the bridge, respectively, requiring the same virtual loading node of the bridge for two times the influence line loading, which can be achieved by controlling the moving speed of the loading vehicle and extracting and recording the two deflection response data.

(3) Find the lowest common multiple A_1 and A_2 of the equivalent concentrated force F_{f1} and F_{f2} of the front axles of the two vehicles; then, amplify the difference after the equivalent concentrated force of the rear axles of the two vehicles by the corresponding magnification, and $\left|A_1F_{f1} - A_2F_{f2}\right|$ is the equivalent loading concentrated force. The deflection data D_{i11} and D_{i12} measured two times are amplified, and then the deflection response $|A_1D_{i11} - A_2D_{i12}|$ corresponding to the concentrated force loading is obtained, which can be used to diagnose bridge damage.

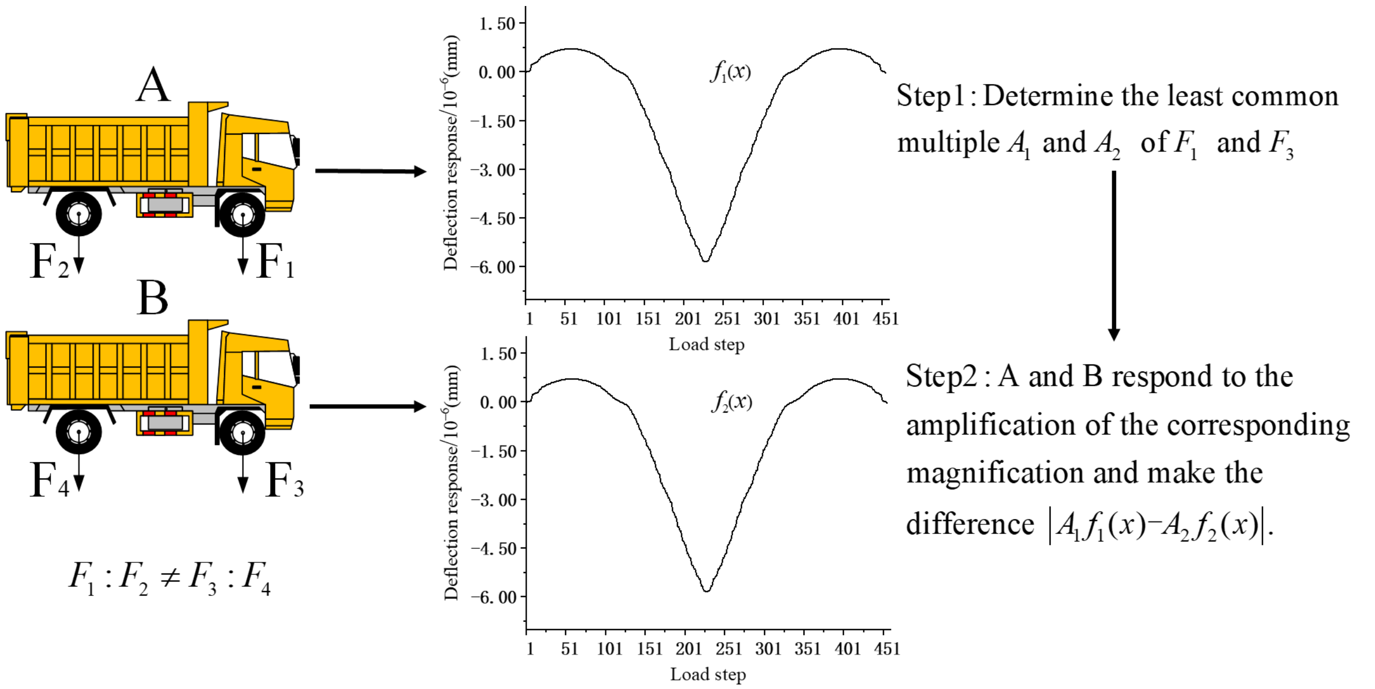

Figure 30. Practical process operation steps.

7. Conclusions

(1) The deflection influence line analytical solution of the hingeless arch in non-damaged condition is derived. It is found that the error of the analytical solution is up to 5.973% when the axial force is considered. The analytical solution can meet engineering precision requirements.

(2) The DILDC solution before and after structural damage was derived, and the feasibility of damage identification of a hingeless arch structure by deflection influence line differential curvature was proved theoretically. It is verified by FE analysis software.

(3) In actual engineering, damage amplitude can be determined by the DILDC; afterwards, the DILDC amplitude curve under different damage conditions can be simu-

lated by FE software, and the damage extent and amplitude relationship formula can be fitted to invert the damage extent so as to achieve accurate damage quantification.

(4) The results show that the amplitude of DILDC index curve is proportional to the damage extent, and the DILDC index has a good effect on the identification of single-location and multiple-location damage of the arch bridge.

(5) The research in this paper contributes to the development of damage diagnosis and load capacity assessment methods for arch bridges. With a combination of existing bridge monitoring methods, the identification method of arch-bridge damage proposed in this paper has the prospect of facilitating routine health assessment of in-service arch bridges in the future.

Author Contributions: Conceptualization, Y.Z.; Formal analysis, M.L.; Methodology, C.X.; Writing—original draft, M.L. and C.X.; Software, M.L., C.X. and D.Z.; Validation, Y.S. and M.Z.; Writing—review and editing, D.Z. All authors have read and agreed to the published version of the manuscript.

Funding: This research was funded by the Natural Science Foundation youth project of Anhui Province (No. 2008085QE247), University Outstanding Top Talent Cultivation Project of Anhui Province (No. gxgnfx2022021), University Scientific Research Major Project of Anhui Province (No. 2022AH050248), Foundation of National and Local Joint Engineering Laboratory of Building Health Monitoring and Disaster Prevention Technology (No. GG22KF002), and Construction Technology Project Plan of Gansu Province (No. JK2023-03).

Data Availability Statement: The data presented in this study are available on request from the corresponding author. The data are not publicly available due to research is continuing.

Conflicts of Interest: Author Chengchao Xu was employed by the company Hefei Zezhong City Intelligent Technology Co., Ltd. The remaining authors declare that the research was conducted in the absence of any commercial or financial relationships that could be construed as a potential conflict of interest.

References

1. Yang, J.F.; Huang, L.; Tong, K.; Tang, Q.; Li, H.; Cai, H.; Xin, J. A Review on Damage Monitoring and Identification Methods for Arch Bridges. *Buildings* **2023**, 13. [CrossRef]
2. An, Y.; Chatzi, E.; Sim, S.H.; Laflamme, S.; Blachowski, B.; Ou, J. Recent progress and future trends on damage identification methods for bridge structures. *Struct. Control Health Monit.* **2019**, *26*, e2416. [CrossRef]
3. Chen, B.C.; Liu, J.P. Review of construction and technology development of arch bridges in the world. *J. Traffic Transp. Eng.* **2020**, *20*, 27–41.
4. He, W.Y.; Ren, W.X.; Zhu, S.Y. Damage detection of beam structures using quasi-static moving load induced displacement response. *Eng. Struct.* **2017**, *145*, 70–82. [CrossRef]
5. Yi, T.H.; Zheng, X.; Yang, D.H.; Li, H.N. Lightweight design method for structural health monitoring system of short- and medium-span bridges. *J. Vib. Eng.* **2023**, *36*, 458–466. (In Chinese)
6. Zheng, X.; Yi, T.H.; Yang, D.H.; Li, H.N. Stiffness Estimation of Girder Bridges Using Influence Lines Identified from Vehicle-Induced Structural Responses. *J. Eng. Mech.* **2021**, *147*, 04021042. [CrossRef]
7. Cheng, X.X.; Song, Z.Y. Modal experiment and model updating for Yingzhou Bridge. *Structures* **2021**, *32*, 746–759. [CrossRef]
8. Gonçalves, M.S.; Carraro, F.; Lopez, R.H. A B-WIM algorithm considering the modeling of the bridge dynamic response. *Eng. Struct.* **2021**, *228*, 111533. [CrossRef]
9. Zhou, Y.; Di, S.K.; Xiang, C.S.; Li, W.; Wang, L. Damage Identification in Simply Supported Bridge Based on Rotational-Angle Influence Lines Method. *Trans. Tianjin Univ.* **2018**, *24*, 587–601. [CrossRef]
10. Wang, N.B.; Zuo, Q.; Li, J.; Huang, T.L. Damage detection method for statically indeterminate bridge based on multi-influence line information in current state. *J. Cent. South Univ. (Sci. Technol.)* **2021**, *52*, 3284–3294. (In Chinese)
11. Fan, C.C.; Zheng, Y.X.; Wang, B.L.; Zhou, Y.; Sun, M. Damage identification method for tied arch bridge suspender based on quasi-static displacement influence line. *Mech. Syst. Signal Process.* **2023**, *200*, 110518. [CrossRef]
12. Wang, N.B.; Wang, C.; Zhou, H.; Zuo, Q. A novel extraction method for the actual influence line of bridge structures. *J. Sound Vib.* **2023**, *553*, 117605. [CrossRef]
13. Zhang, G.W.; Zhao, W.J.; Zhang, J. Bridge distributed rigidity identification of continuous beam bridge based on microwave interferometric radar technology and rotation influence line. *Measurement* **2023**, *220*, 113353. [CrossRef]
14. Zhu, J.S.; Zhang, C.; Li, X.T. Structural damage detection of the bridge under moving loads with the quasi-static displacement influence line from one sensor. *Measurement* **2023**, *211*, 112599. [CrossRef]
15. He, W.Y.; Li, Z.D.; Zhou, L.; Ren, W.-X.; Li, Y. The effect of environmental temperature on influence line of concrete beam type bridge. *Structures* **2023**, *48*, 1468–1478. [CrossRef]

16. Mustafa, S.; Yoshida, I.; Sekiya, H. An investigation of bridge influence line identification using time-domain and frequency-domain methods. *Structures* **2021**, *33*, 2061–2065. [CrossRef]
17. Ge, L.; Koo, K.Y.; Wang, M.; Brownjohn, J.; Dan, D. Bridge damage detection using precise vision-based displacement influence lines and weigh-in-motion devices: Experimental validation. *Eng. Struct.* **2023**, *288*, 116185. [CrossRef]
18. Nady, H.O.; Mohamed, A.B.; Abdo; Kaiser, F. Comparative study of using rotation influence lines and their derivatives for structural damage detection. *Structures* **2023**, *48*, 397–409. [CrossRef]
19. Feng, Q.; Wei, P.; Lou, J.B.; Cai, J.; Xu, R. Analytical solution for quick decision of tied–arch bridge parameters at early-design stage based on Hellinger–Reissner variational method. *Structures* **2022**, *44*, 1443–1453. [CrossRef]
20. Hejazi, M.; Mehdian, A. Experimental and numerical investigation on masonry arch bridges under uniform and line loads. *Structures* **2023**, *47*, 665–680. [CrossRef]
21. You, R.Z.; Yi, T.H.; Ren, L. Equivalent estimation method (EEM) for quasi-distributed bridge-deflection measurement using only strain data. *Measurement* **2023**, *221*, 113492. [CrossRef]
22. Bowen, L.; Anastasios, D.; Vasilis, S. A material characterisation framework for assessing brickwork masonry arch bridges: From material level to component level testing. *Constr. Build. Mater.* **2023**, *397*, 132347.
23. Soleymani, A.; Jahangir, H.; Nehdi, M.L. Damage detection and monitoring in heritage masonry structures: Systematic review. *Constr. Build. Mater.* **2023**, *397*, 132402. [CrossRef]
24. Doeva, O.; Masjedi, P.K. Exact analytical solution for static deflection of Timoshenko composite beams on two-parameter elastic foundations. *Thin-Walled Struct.* **2022**, *172*, 108812. [CrossRef]
25. Shuo, W.; Farhad, H.; Casero, M.; Obrien, E.J.; Fidler, P.; McCrum, D.P. A Novel Bridge Damage Detection Method Based on the Equivalent Deflection Influence Lines–Theoretical Basis and Field Validation. *SSRN* **2023**, *31*, 110738.
26. Zhou, Y.; Di, S.K.; Xiang, C.S.; Wang, L. Damage Detection for Simply Supported Bridge with Bending Fuzzy Rigidity Consideration. *J. Shanghai Jiaotong Univ. (Sci.)* **2018**, *23*, 308–319. [CrossRef]
27. Xiang, C.S.; Liu, H.L.; Liu, C.Y.; Zhou, Y.; Wang, L.-X.; Memmolo, V. Structure Damage Identification Based on Information Entropy and Bayesian Fusion. *Math. Probl. Eng.* **2022**, *2022*, 1–19. [CrossRef]
28. Wang, X.J.; Chen, F.; Zhou, H.Y.; Ni, P.; Wang, L.; Zhang, J. Structural damage detection based on cross-correlation function with data fusion of various dynamic measurements. *J. Sound Vib.* **2022**, *541*, 117373. [CrossRef]
29. Wang, N.B.; Shen, W.; Guo, C.R.; Wan, H.P. Moving load test-based rapid bridge capacity evaluation through actual influence line. *Eng. Struct.* **2022**, *252*, 113630. [CrossRef]
30. Wang, J.J.; Chen, M.; Yin, C.B. Test and research of long-term stress variation of high-pier and long-span continuous rigid-frame bridge. *Adv. Mater. Res.* **2013**, *639–640*, 269–273. [CrossRef]